

**COHERENTLY DISTRIBUTED RF ANTENNA ARRAYS USING PHOTONIC  
LINKS**

by

Shadia Islam Chowdhury

A thesis submitted to the Faculty of the University of Delaware in partial fulfillment  
of the requirements for the degree of Master of Science in Electrical and Computer  
Engineering

Fall 2025

© 2025 Shadia Islam Chowdhury  
All Rights Reserved

**COHERENTLY DISTRIBUTED RF ANTENNA ARRAYS USING PHOTONIC  
LINKS**

by

Shadia Islam Chowdhury

Approved: \_\_\_\_\_  
Dennis W. Prather, Ph.D.  
Professor in charge of thesis on behalf of the Advisory Committee

Approved: \_\_\_\_\_  
Hui Fang, Ph.D.  
Chair, Department of Electrical and Computer Engineering

Approved: \_\_\_\_\_  
Pamela M. Norris, Ph.D.  
Dean of the College of Engineering

Approved: \_\_\_\_\_  
Gary T. Henry, Ph.D.  
Interim Vice Provost and Dean of the Graduate College

## ACKNOWLEDGMENTS

*“I am not afraid of storms, for I am learning how to sail my ship.”*

– Louisa May Alcott

I owe my deep gratitude to my advisor, Dr. Dennis Prather, for welcoming me into his group in 2022 and for providing me with the guidance, tools, and environment I needed to grow as a researcher. I am grateful for his constant encouragement, challenging me to think beyond short-term goals, and giving me the resources and support that helped me develop both as a student and as a researcher. I also appreciate the supportive and collaborative group environment he has created, which has allowed me to improve my research and presentation skills.

I am also very thankful to Dr. Shouyuan Shi for his mentorship throughout this project. His guidance, support, and approachable attitude made a big difference in my work. I would like to express my gratitude to Drs. Xiao-Feng Qi, Janusz Murakowski, and Garrett Schneider for the many helpful discussions, thoughtful suggestions, and different perspectives they shared during meetings. I also thank the members of Phase Sensitive Innovations for their support, answering my questions, and providing resources when needed. I am equally grateful to all the members of the Prather group for their help and creating a friendly and encouraging work environment. In particular, I want to thank Dr. Hannah Sinigaglio for helping me in my early days to set up my experiments, navigate coursework, share materials, and offer guidance whenever I needed it.

Finally, I would like to thank my parents and siblings for their unconditional support. Their encouragement has helped me make difficult decisions, stay motivated, and continue to grow throughout this journey.

## TABLE OF CONTENTS

LIST OF TABLES .....	vii
LIST OF FIGURES .....	viii
ABSTRACT .....	x
Chapter	
1 INTRODUCTION .....	1
1.1 RF-Photonic System .....	2
1.2 Contributions .....	4
1.3 Thesis Organization .....	5
2 HOLOGRAM DESIGN FOR COHERENTLY DISTRIBUTED ANTENNA SYSTEM .....	8
2.1 Holographic MIMO for Communication .....	8
2.2 Mathematical Formulation .....	10
2.3 Simulation Results .....	11
2.3.1 Single Array, a.k.a. Massive MIMO .....	12
2.3.1.1 MRT & ZF Precoder Design .....	13
2.3.2 Unconstrained Distribution of Subarrays .....	15
2.3.3 Unconstrained Distribution of Elements .....	16
3 SYSTEM OVERVIEW .....	18
3.1 Photonic Processing Unit .....	18
3.1.1 Tunable Optical Paired Source (TOPS) .....	19
3.1.2 Feed Network .....	20
3.2 Complex Weighting Matrix .....	20
3.3 Remote RF Frontend .....	21
4 EXPERIMENTAL BUILDING BLOCKS .....	22

4.1	Transmitter Cart Software Overhaul .....	22
4.2	Transmitter Hardware Fixes and Testing .....	26
4.3	True Time Delay (TTD) Units .....	27
4.4	Anechoic Enclosure Plan and Build .....	29
5	RESULTS AND DISCUSSION.....	31
5.1	Experimental Setup .....	31
5.2	Interference Pattern for Various Phase Distributions .....	34
5.2.1	$V_{2\pi}$ Estimation & Measurement .....	36
5.2.2	Near - field Phase Compensation .....	37
5.2.3	Beamforming & Beam Steering at Different location.....	38
5.3	Phase Coherence vs Incoherence Transmission across Antennas .....	40
5.4	Maintenance of Phase Coherence with Differential Fiber Lengths.....	41
6	FUTURE WORK .....	43
6.1	Beamforming with Multiple Users in Distributed Antenna System .....	43
6.2	Incorporating Data Modulation on the Coherent Optical Carriers .....	44
7	CONCLUSION .....	45
	REFERENCES .....	47
	Appendix	
A	PUBLICATION LIST .....	51

## LIST OF TABLES

Table 5.1 Simulation & Experimental Parameters .....	33
Table 5.2 Measured Power and Current Levels at System Key Points .....	34

## LIST OF FIGURES

Figure 2.1. Photonically enabled distributed Tx antenna array for in-plane RF holograms (ROI: Region of Interest).....	9
Figure 2.2. Simulation setup showing the normalized power profile (linear scale) for beamforming toward two users located at $(x, y) = (0, -3)$ and $(0, 3)$ using a 16-element linear antenna array.....	13
Figure 2.3. Received power comparison between MRT and ZF precoders for two users. (a) radiation pattern shows peak at user <sub>1</sub> position $(x_1, y_1) = (0, -3)$ & null at user <sub>2</sub> position $(x_2, y_2) = (0, 3)$ ; (b) radiation pattern shows null at user <sub>1</sub> position $(x_1, y_1) = (0, -3)$ & peak at user <sub>2</sub> position $(x_2, y_2) = (0, 3)$ .....	14
Figure 2.4. Simulation setup showing the normalized power profile (linear scale) for beamforming toward two users located at $(x, y) = (0, -3), (0, 3)$ . (a) evenly spaced four-array linear configuration with 16 elements ; (b) circularly distributed array configuration with 16 elements. ....	16
Figure 2.5. Simulation setup showing the normalized power profile (linear scale) for 16 antenna elements uniformly distributed on a circle of radius $9.35\lambda$ for beamforming analysis.....	17
Figure 3.1. System diagram of distributed TX antenna. (TOPS: Tunable Optical Paired Source; LO: Local Oscillator; PMF: Polarization-Maintaining Fiber; PBC: Polarization Beam Combiner; PM: Phase Modulator; LP: Linear Polarizer ; EDFA: Erbium-Doped Fiber Amplifier ; VOA: Variable Optical Attenuator; PD: Photo Detector; PA: Power Amplifier; LNA: Low-Noise Amplifier; ESA: Electronic Spectrum Analyzer).....	19
Figure 4.1. Schematic diagram of the TX system in the LabVIEW interface.....	23
Figure 4.2. LabVIEW “Start Here” panel showing initialization options for TOPS and feed networks, channel calibration selection, and motion control setup for the transmitter unit. ....	24

Figure 4.3. LabVIEW panel showing phase and amplitude calibration control panels used to adjust VOAs and synchronize phase across all transmitter channels.....	25
Figure 4.4. Assembled PD and TSA antenna unit in a custom 3D printed holder with antenna radiation pattern. ....	27
Figure 4.5. Left: A true time delay (TTD) box with lid on. Right: inside view of the enclosure.....	28
Figure 4.6. Anechoic enclosure made from foam boards, movable room dividers, pyramidal microwave absorber and antenna setup.....	30
Figure 5.1. System measurement setup for the experimental performance analysis....	32
Figure 5.2. Performance comparison between simulation and lab experiment in terms of interference pattern for various phase ( $\phi$ ) distributions in degrees. ....	35
Figure 5.3. $V2\pi$ measurement based on least squared error estimation; (a) $2\pi$ phase sweep with incorrect $V2\pi$ set to the system; (b) $2\pi$ phase sweep with correct $V2\pi$ set to the system. ....	36
Figure 5.4. Near-field phase compensation; (a) beamforming “without” near-field phase compensation, (b) beamforming “with” near-field phase compensation. ....	38
Figure 5.5. Performance comparison between simulation and lab experiment in terms of interference pattern for various beamforming location. (a) beam formed at the center (0 cm); (b) beam steered to +5 cm; (c) beam steered to +10 cm; (d) beam steered to -15 cm; (e) beam steered to +15 cm.....	39
Figure 5.6. Performance comparison showing phase coherence versus incoherence transmission across five TX antennas. ....	40
Figure 5.7. Performance comparison showing maintenance of phase coherence with differential fiber lengths. ....	41

## ABSTRACT

This thesis presents a coherently distributed multiple-input multiple-output (MIMO) radio-frequency (RF)-photonic system operating at millimeter wave (mmWave) frequencies. Over long distances with negligible propagation loss, this system uses radio-frequency-over-fiber (RFoF), or RF-photonic links, to implement distributed antenna system that preserves both the spatial and temporal coherence of RF signals. It utilizes the principles of photonic signal generation and the distribution of RF signals using a centralized optical local oscillator (OLO) to maintain phase and frequency coherence across antennas separated by tens of kilometers. Based on the proposed RF-photonic system architecture, this thesis presents the development and simulation of various antenna configurations, including single-array architectures, unconstrained distributions of subarrays and individual elements. These configurations are analyzed as proof-of-concept demonstrations to validate the precoding strategies, including zero forcing (ZF) and maximal ratio transmission (MRT), and their performance is evaluated using a simulation precoder design algorithm to establish the feasibility of the overall system design.

This RF-photonic system also includes a photonic processing unit (PPU) that contains a tunable optical paired source (TOPS), photonic feed network that enables a complex weighting matrix, which enables phase and amplitude control in the optical domain to apply beamforming weights, and finally high-power photodiodes (PDs) in the remote RF frontend. The system is used to implement optimized complex weights, on distributed antenna elements, to realize “flat,” i.e., lying in the plane of

propagation, holographic field profiles. In order to implement the practical performance of the holographic field profiles in the phase-synchronized distributed beamforming systems, hardware and software development are carried out. This distributed beamforming system includes the implementation of the transmitter (Tx) module, including both the software framework developed in LabVIEW and hardware enhancements achieved through the integration of supplementary test equipment for improved data acquisition and system monitoring.

Various calibration techniques are used to obtain far-field radiation patterns and to maintain phase coherence across multiple distributed antennas. Experimental validation of a one-dimensional indoor system is used to demonstrate the aforementioned “in-plane” holograms, along with their comparison to simulation results. The experimental implementation and validation of various precoding schemes are utilized to implement the long range distribution of RF signals without being limited by cable loss. The proposed system preserves coherence even with differential fiber lengths to the different remote antennas. This system can be expanded to support multiple users by increasing the number of transmit antennas and incorporating data modulation on the coherent carriers. With these advancements, full system-level performance evaluation including data rate, spectral efficiency and bit error rate is planned for future work.

## Chapter 1

### INTRODUCTION

The integration of sensing into 5G and 6G wireless communication systems has drawn interest in new technologies to achieve both high resolution imaging and sensing [1] and high data rate communications [2], [3]. In particular, phased arrays enable radio-frequency (RF) systems to perform both functions simultaneously by allowing individual beams to be steered to specific receivers or receive signals from multiple transmitters at different locations, different frequencies, and with different functions.

Fourier-based opto-electronically driven phased arrays have been developed that, when combined with conventional technologies, preserve the spatial and temporal coherence of the RF field [4], [5], [6]. To achieve this, the demonstrated photonic system implements in real-time the fundamental holographic principle of encoding the spatial amplitude and phase of gigahertz electro-magnetic fields on an optical carrier, referred to as holographic multiple input multiple output (H-MIMO), which is an emerging technique gaining significant interest in next generation wireless systems. This technique involves the integration of many small and affordable antenna elements across a distributed space, resulting in a spatially distributed aperture. MIMO technology has developed into several subcategories, such as network MIMO [7], distributed MIMO, cooperative MIMO [8], coordinated multipoint (CoMP), and others, based on the efficient use of the current equipment and application to certain scenarios. This MIMO techniques enables operation across multi-gigahertz

bandwidths, delivering both enhanced spectral utilization and improved power efficiency, which are vital for accommodating the continuously increasing throughput demands of modern wireless infrastructures [9], [10]. Nevertheless, expanding these systems introduces considerable difficulties related to hardware scalability and environmental requirements, especially given that line-of-sight (LoS) propagation is less likely to be available when a single co-located linear array is used to support multiple users within a cell or scene [11]. To mitigate these challenges, distributed MIMO configurations have been proposed as viable solutions for achieving improved system performance.

To further improve system coverage and resilience to channel state variations, multiple spatially distributed H-MIMO apertures can cooperate in a temporally and spatially-coherent manner to jointly form beams and field patterns to/from one or more objects using the same frequency, simultaneously. For this reason, such distributed beamforming, with real-time updates, can overcome dynamic blockage in real-world scenarios, hence enabling more resilient operations. In practice, RF phase coherence must be maintained over tens of kilometers in a cloud-centric network in order to increase the effective spatial resolution of the system.

## **1.1 RF-Photonic System**

To enhance the distributed mmWave network, we propose an RF-photonic system that utilizes the photonic generation and distribution of RF signals. While single-frequency mmWave radio-over-fiber (RoF) has been demonstrated, the distribution of RF signals in line-of-sight applications [12], current all-electronic cabling between the base station and remote radios falls short of ensuring distributed coherence over long-distances with minimum power loss. Recently, a technology has

been demonstrated that allows for the coherent up-conversion of an RF signal, incident on an RF receiver antenna aperture, to the optical domain [13], in such a way as to preserve the RF phase front. In addition, because the RF phase front is up-converted to the optical domain, all of the beamspace processing can be performed using a Fourier transform lens with near-zero latency and unlimited beam-bandwidth product. This capability enables real-time RF sensing, imaging, and real-time RF wavefront generation in a remote and/or distributed antenna system, as reported herein.

In distributed beamforming operation, it is essential that each transmitted signal reaches the intended destination synchronously and with the appropriate amplitude and phase profile. This allows the radiated signals to combine constructively and thereby form regions of improved signal-to-noise ratio (SNR). Additionally, for receiving operation, it ensures that the corresponding signals coincide for coherent beamspace signal processing using Fourier optics [14]. When transmitting signals in a distributed coherent system, it is challenging to align the electrical weights of each antenna element and maintain synchronization in real-time [3], which is necessary for coordinated beamforming and to realize beam patterns in such a distributed system [15], [16], [17], [18]. In this case, it is feasible to precisely align all of the signals to maximize gain for a specific user or, in the case of H-MIMO, multiple simultaneous users. Additionally, when such signals are optimized they can introduce nulls for unintended users thereby minimizing interference, hence maximizing the signal-to-interference-plus-noise ratio (SINR) [6].

To demonstrate such a distributed mmWave antenna network, we utilize an RF-photonic system that employs photonic generation and distribution of RF signals. This approach enables high-speed, high-frequency microwave communications to be

realized using low-loss optical fiber and high-bandwidth optical components. It also offers advantages for other applications, notably low-loss transmission, reduced phase noise, lightweight, ultra-wideband operation, distributed coherence as well as concurrent multi-beam, and multi-band performance [14], [19].

Preliminary work established the feasibility for remoting two transmitters over large distances while maintaining mutual phase coherence with negligible loss of signal power, as demonstrated in an RF version of “Young’s Double Slit ” experiment using mmWave signals with a path length differential of up to 45 kilometers [20]. Recently this work expanded on these experiments to coherently distributed beamforming from five transmitters, with adjustable phase and amplitude profiles designed to form requisite power distributions at suitable distances and implemented in the optical domain [21]. Unlike conventional all-RF architectures, the optical approach supports a significantly broader RF bandwidth and enables the delivery of a centralized optical local oscillator (LO) signal to remote radio units located several kilometers apart. This capability ensures phase alignment across spatially distributed access points (Aps), enabling phase-and frequency-coherent signal transmission to user equipments (UEs) served by APs spread over a large geographic area [14], [22], [23].

## **1.2 Contributions**

The major contributions of this work are summarized as follows:

- Development of a coherent RF-photonic phased array system:

Design and implement an RF-photonic phased array architecture that is capable of distributing high-frequency RF signals over an optical fiber network while maintaining phase coherence across spatially separated antenna elements. Demonstrate

that radio-frequency-over-fiber (RFoF) distribution enables long-distance deployment of antennas without suffering the phase drift and cable losses typically observed in conventional RF links.

- Centralized control using a common optical LO:

A centralized optical LO distribution scheme, ensuring that all remote antenna units share a common phase-locked reference. This configuration minimizes synchronization errors, enhances beamforming accuracy, and provides a scalable solution for large, distributed antenna arrays.

- Simultaneous multi-band and multi-beam transmission capability:

The proposed photonic architecture supports simultaneous multi-band, multi-beam transmission over wide bandwidths with a high beam-bandwidth product, overcoming the complexity and spectral limitations of all-RF systems.

- Experimental demonstration and validation of theoretical models:

Conduct comprehensive experimental validation using a practical downlink testbed to verify simulation and analytical predictions. Demonstrate coherent beam combining at the user and confirming stable phase alignment across all optical links. Successfully generate and steer multiple beam patterns, verifying precise control of main-lobe and null positions. The experimental outcomes confirm the feasibility and robustness of the proposed photonic transmission system for distributed coherent beamforming applications.

### **1.3 Thesis Organization**

This thesis is organized as follows.

Chapter 2 presents the overall design concept of an in-plane RF hologram operating in the mmWave spectrum, along with the mathematical framework for a

coherently distributed antenna system. This chapter introduces the principles of photonic signal generation and distribution of the RF signals used for analog beamforming. It further details the development and simulation of various distributed antenna configurations, including single-array architectures, as well as unconstrained distributions of subarrays and individual elements. These configurations are analyzed as proof-of-concept demonstrations to validate the proposed precoding strategies, including zero forcing (ZF) and maximal ratio transmission (MRT), and evaluates their performance in simulation precoder design algorithms to establish the feasibility of the overall system design.

Chapter 3 presents the RF-photonic system architecture for the transmitter which includes the photonic processing unit (PPU) containing the tunable optical paired source (TOPS) and feed network, followed by the complex weighting matrix, which enables phase and amplitude control in the optical domain to apply beamforming weights and finally the remote RF frontend. This chapter explains how both phase and frequency coherence are maintained across the system to ensure coherent combining at the user.

Chapter 4 presents the hardware integration and software development carried out to evaluate the practical performance of phase-synchronized distributed beamforming systems. It details the implementation of the transmitter (Tx) module, including both the software framework developed in LabVIEW and the hardware enhancements achieved through the integration of supplementary test equipment for improved data acquisition and system monitoring. To enable future experimental studies, custom true time delay (TTD) modules and a dedicated anechoic testing environment are also designed and assembled. This chapter provides a comprehensive

overview of these developments, establishing the foundation for subsequent experimental validation and performance analysis.

Chapter 5 describes the experimental setup incorporating the key components required for coherent RF signal distribution, including the TOPS and high-power photodiodes (PDs). This chapter introduces various calibration techniques used to obtain far-field radiation patterns and to maintain phase coherence across multiple distributed antennas. It also presents a detailed performance analysis demonstrating the formation of in-plane RF holograms, with experimental results compared with simulations.

Chapter 6 outlines future research directions, while Chapter 7 concludes the thesis by summarizing key findings and contributions.

## Chapter 2

### HOLOGRAM DESIGN FOR COHERENTLY DISTRIBUTED ANTENNA SYSTEM

This chapter presents a photonicly enabled distributed MIMO system designed to maintain phase coherence across spatially separated antenna arrays to achieve coherent signal combining at the user end. It introduces the design concept of an in-plane RF hologram operating in the mmWave spectrum, along with the mathematical formulation for a coherently distributed antenna framework. Furthermore, the chapter explores various antenna orientations and array configurations to implement and analyze precoding techniques such as MRT and ZF through simulation studies, providing insights into their impact on beamforming performance and interference suppression.

#### 2.1 Holographic MIMO for Communication

To design an in-plane RF hologram in the mmWave spectrum, it is essential to maintain phase coherence across distributed antenna arrays with arbitrary locations. Herein, we present a photonicly-enabled distributed Tx antenna array in Figure 2.1, that preserves phase coherence between antennas or multiple subarrays across distributed locations using an RF-photonic system. By generating signals photonicly, precise phase and amplitude weights can be applied to individual transmit elements, similar to the amplitude and phase weights used in computer-generated holograms (CGHs) [24], but in the RF domain.

These complex weights are necessary for generating intricate beam patterns required for two-dimensional in-plane RF holograms. Such control can be achieved over a wide operational bandwidth by using photonic components, such as electro-optic modulators (EOMs), with optically phase-locked paired signals [25] that generate and manage RF communication signals in the optical domain. The continuous adjustment of amplitude and phase allows for the realization of an in-plane RF hologram profile wherein the far-field radiation pattern is optimized to the overall needs of the channel state of the wireless communication system. While Figure 2.1 provides an overview of the process with the mathematical explanation to realize the system response, a more detailed visualization and analysis can be found in Figure 3.1 of Chapter 3, which offers a closer depiction of its key components/features.

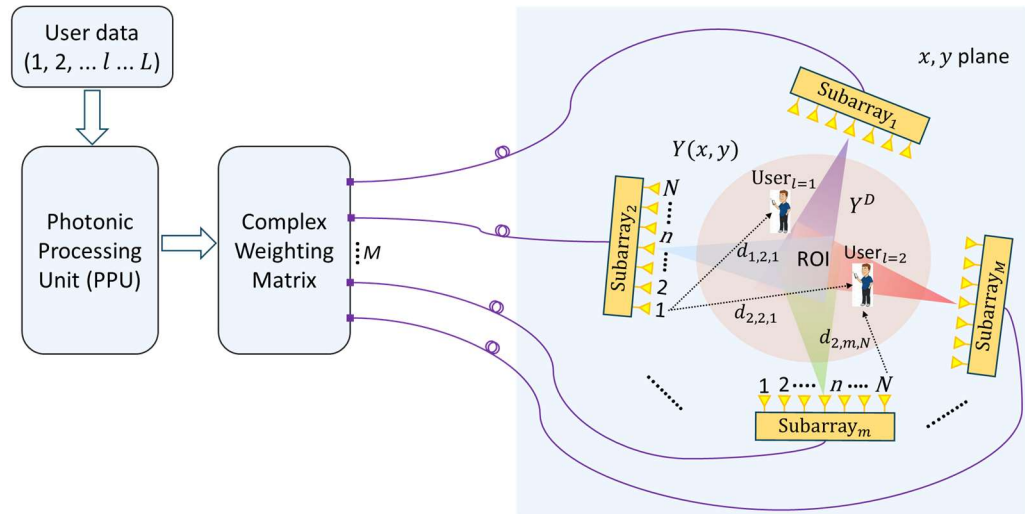


Figure 2.1. Photonically enabled distributed Tx antenna array for in-plane RF holograms (ROI: Region of Interest).

## 2.2 Mathematical Formulation

Using this approach, the goal is to realize a two-dimensional in-plane RF hologram in the  $x, y$  plane, where  $L$  users are served with  $L$  independent data streams in Figure 2.1. The system radiation response at a given coordinate  $x, y$  within the region of interest is defined as  $Y(x, y)$ , and  $Y^D$  denotes the desired response to form the beams toward  $L$  users.

This system is considered to be equipped with  $M$  transmit subarrays with each array having  $N$  antenna elements to serve a total of  $L$  users. The propagation response from the  $n^{\text{th}}$  element of the  $m^{\text{th}}$  subarray to the  $l^{\text{th}}$  user, in the region of interest can be expressed as

$$p_{l,m,n} = \frac{e^{jkd_{l,m,n}}}{d_{l,m,n}}. \quad (2.1)$$

Note that  $d_{l,m,n}$  is the distance calculated as  $d_{l,m,n} = \sqrt{(x_l - x_{m,n})^2 + (y_l - y_{m,n})^2}$ , and  $k = \frac{2\pi}{\lambda}$  is the propagation constant.

The propagation response vector  $\mathbf{p}_l \in \mathbb{C}^{MN \times 1}$  for the  $l^{\text{th}}$  user can be written as,  $\mathbf{p}_l = [p_{l,1,1}, p_{l,1,2}, \dots, p_{l,1,N}, p_{l,2,1}, \dots, p_{l,M,N}]^T$ . Furthermore, the total propagation response matrix  $\mathbf{P} \in \mathbb{C}^{MN \times L}$  from  $MN$  transmit antenna elements to  $L$  users can be expressed as,  $\mathbf{P} = [\mathbf{p}_1, \mathbf{p}_2, \dots, \mathbf{p}_l \dots, \mathbf{p}_L]$ .

To achieve the desired radiation pattern to the  $l^{\text{th}}$  user within the region of interest,  $w_{l,m,n}$  is the distributed transmit complex weight for  $n^{\text{th}}$  element of the  $m^{\text{th}}$  subarray. Note that  $w_{l,m,n}$  can be expressed as  $|w_{l,m,n}| e^{j\phi_{l,m,n}}$ . To render the appropriate  $w_{l,m,n}$ , phase controllers and variable optical attenuators (VOAs) are used to realize  $\phi_{l,m,n}$  and  $|w_{l,m,n}|$ , respectively, and the complex weight matrix  $\mathbf{W} \in \mathbb{C}^{MN \times L}$  can be written as:

$$\mathbf{W} = \begin{bmatrix} w_{1,1,1} & w_{2,1,1} & \cdots & w_{L,1,1} \\ w_{1,1,2} & w_{2,1,2} & \cdots & w_{L,1,2} \\ \vdots & \vdots & \vdots & \vdots \\ w_{1,1,N} & w_{2,1,N} & \cdots & w_{L,1,N} \\ w_{1,2,1} & w_{2,2,1} & \cdots & w_{L,2,1} \\ \vdots & \vdots & \vdots & \vdots \\ w_{1,M,N} & w_{2,M,N} & \cdots & w_{L,M,N} \end{bmatrix} \quad (2.2)$$

The combined propagation response  $\mathbf{Y}^D \in \mathbb{C}^{L \times L}$  for  $MN$  transmit antenna elements and  $L$  users can be formed as

$$\mathbf{Y}^D = \mathbf{W}^T \mathbf{P}. \quad (2.3)$$

### 2.3 Simulation Results

To evaluate the performance of arbitrary antenna positioning, simulations are performed using MATLAB, wherein multiple users are randomly placed within the region of interest (ROI). Unlike a conventional all-RF MIMO transmitter, the proposed RF-photonic transmitter first up-converts the baseband signal to the optical domain using an EOM. Analog MIMO beamforming (precoding) is then performed in the optical domain before the signal is down-converted back to RF through a photodetector (PD). This optical beamforming approach enables a significantly higher beam-bandwidth product (BBP) [14], while allowing centrally precoded signals to be distributed to remote transmitters over long distances with minimal loss and maintaining RF phase coherence.

Complex precoding schemes, such as conjugate beamforming or MRT and ZF precoding, are applied simultaneously to individual antenna elements by adjusting

both phase and amplitude. This enables the formation of precise beam patterns directed toward the intended user locations [26].

Maximal Ratio Transmission computes the phase and amplitude weights for each user based on the number of transmitting antennas using conjugate beamforming. It focuses on maximizing the received signal power at the intended user location while ignoring inter-user interference, making it suitable for scenarios with low user density or weak interference coupling.

In zero-forcing precoding, the steering vectors for all users are jointly determined from the channel state vectors for the users. The resultant steering vector for each user is orthogonal to the channel vectors of all the other users, thereby creating ‘cold spots’ at the locations of all the users except the target user. For a network of  $N$  number of antennas in a single linear array and  $L$  users,  $L$  degrees of freedom is spent on orthogonalizing between the users, and the remaining  $(N-L)$  degrees of freedom are used to concentrate power to each user. Even though received power for each user is less than that of MRT, the SINR improves markedly, especially for large  $N$ .

### **2.3.1 Single Array, a.k.a. Massive MIMO**

This section presents the simulation results for a linear antenna array consisting of 16 elements, each spaced by one wavelength ( $\lambda$ ). As shown in Figure 2.2, the power distribution is simulated within a  $5\lambda \times 5\lambda$  region of interest (ROI) for an array placed at a distance of  $9.4\lambda$  from the observation field. In these simulations, the phase and amplitude weights for each antenna element are calculated using both MRT and ZF precoding schemes. The beamforming performance is evaluated for two user positions

located at  $(x_1, y_1) = (0, -3)$  and  $(x_2, y_2) = (0, 3)$  to compare how each precoding method influences the resulting radiation pattern and interference suppression.

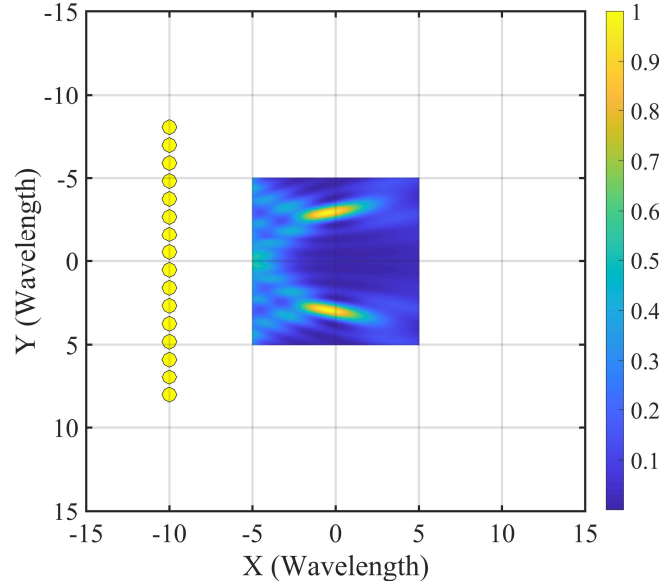


Figure 2.2. Simulation setup showing the normalized power profile (linear scale) for beamforming toward two users located at  $(x, y) = (0, -3)$  and  $(0, 3)$  using a 16-element linear antenna array.

### 2.3.1.1 MRT & ZF Precoder Design

Figure 2.3 illustrates the radiation pattern obtained for two users as a result of beamforming performed by a 16-element linear antenna array. A vertical line scan of 10 cm along  $x = 0$  (as shown in Figure 2.2) is used to visualize the radiation pattern distribution. In this setup, two users are positioned at -3 cm and 3 cm along the vertical axis, corresponding to the cartesian coordinates  $(x_1, y_1) = (0, -3)$  and  $(x_2, y_2) = (0, 3)$ .

In Figure 2.3 (a) and (b), we plot the radiation patterns for different precoding algorithms for two users positioned at -3 cm and 3 cm along the vertical axis. In multi-

user transmission systems, the fundamental aim of a precoder is to improve the spectral efficiency by maximizing the SINR. This is achieved by directing transmission energy toward the desired receiver while minimizing unwanted radiation in other directions to limit interference.

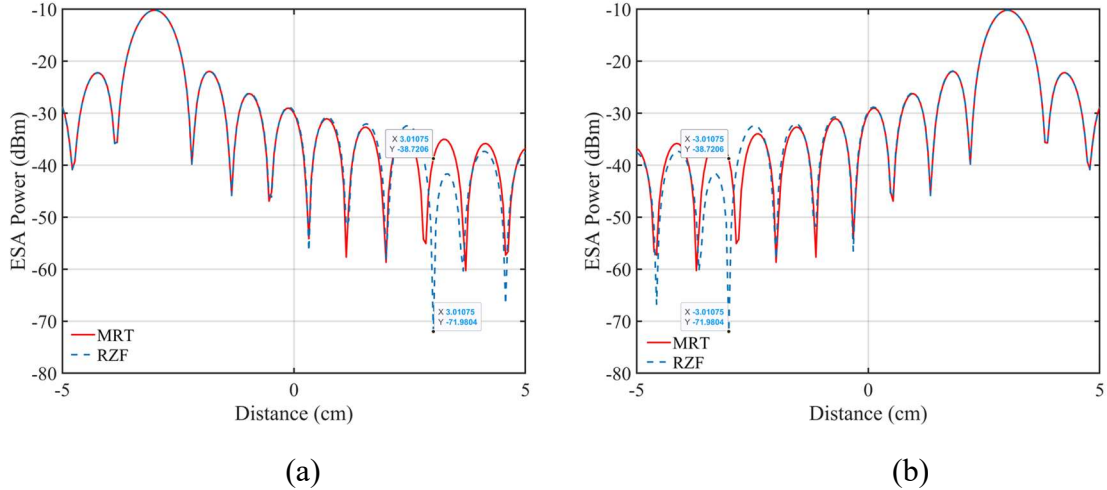


Figure 2.3. Received power comparison between MRT and ZF precoders for two users. (a) radiation pattern shows peak at user<sub>1</sub> position  $(x_1, y_1) = (0, -3)$  & null at user<sub>2</sub> position  $(x_2, y_2) = (0, 3)$ ; (b) radiation pattern shows null at user<sub>1</sub> position  $(x_1, y_1) = (0, -3)$  & peak at user<sub>2</sub> position  $(x_2, y_2) = (0, 3)$ .

Figure 2.3 illustrates the measured field intensity along the  $y$ -axis at  $x = 0$ . An evident intensity peak at -3 cm corresponds to the location of the desired user, confirming effective energy concentration. The comparatively weaker response observed at 3 cm signifies reduced interference at the second user. The distribution pattern for user<sub>1</sub> reveals the contrast between MRT and ZF precoders. The ZF method effectively introduces a null at the location of user<sub>2</sub>, showing better suppression of unwanted coupling between users. In contrast, MRT (also known as conjugate

beamforming) lacks the capability to create such nulls, leading to greater power leakage from user<sub>1</sub> toward user<sub>2</sub> and increased interference. Thus, as observed in Figure 2.3(a) and (b), the ZF approach consistently yields higher SINR and improved bandwidth efficiency compared to MRT.

### 2.3.2 Unconstrained Distribution of Subarrays

The previous section compared the radiation patterns produced by the MRT and ZF precoding methods to illustrate how each approach influences beam direction and interference control. Expanding on that analysis, this section investigates the effect of antenna orientation on beamforming performance. As shown in Figure 2.4(a) and (b), simulations are conducted for two users positioned at  $(x_1, y_1) = (0, -3)$  and  $(x_2, y_2) = (0, 3)$  within a  $5\lambda \times 5\lambda$  ROI. Each configuration consists of 16 antenna elements separated by one wavelength ( $\lambda$ ) and positioned approximately  $9.4\lambda$  from the observation field.

In Figure 2.4(a), the elements are arranged into four linear subarrays, while Figure 2.4(b) presents a circular array configuration. The linear geometry provides a more concentrated main lobe but exhibits higher side-lobe levels near the beam edges. Conversely, the circular arrangement distributes energy more uniformly, maintaining consistent phase coherence across a broader angular span. These findings highlight that array geometry, in addition to the applied precoding technique, significantly affects the beam pattern characteristics, interference behavior, and overall system efficiency.

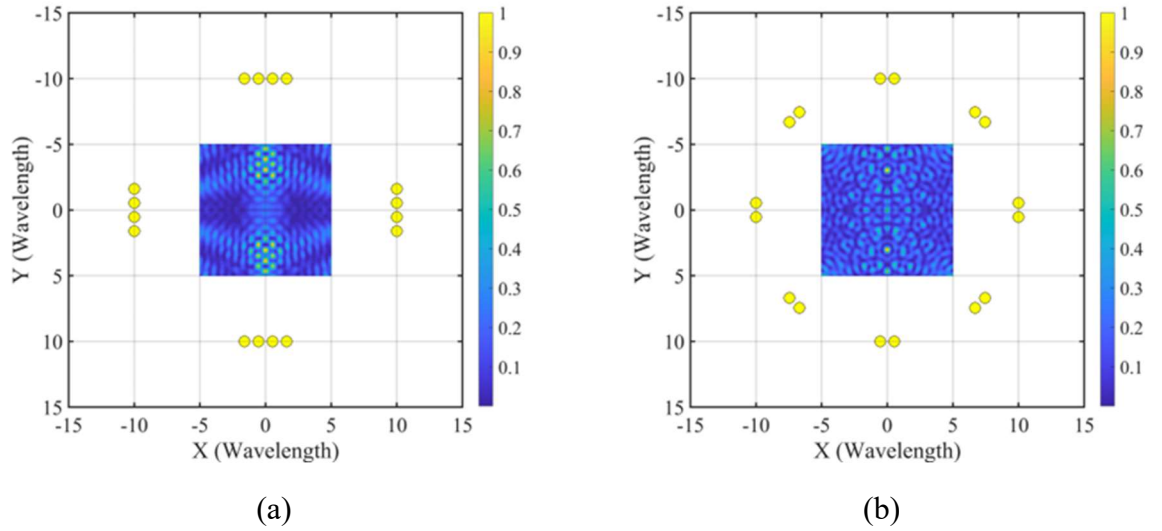


Figure 2.4. Simulation setup showing the normalized power profile (linear scale) for beamforming toward two users located at  $(x, y) = (0, -3), (0, 3)$ . (a) evenly spaced four-array linear configuration with 16 elements ; (b) circularly distributed array configuration with 16 elements.

### 2.3.3 Unconstrained Distribution of Elements

Building on the previous comparison of antenna orientations, Figure 2.5 shows the simulation setup for a circular array composed of 16 antenna elements evenly distributed along a radius of  $9.4\lambda$ . The simulation considers the above mentioned location of two users at  $(x_1, y_1) = (0, -3)$  and  $(x_2, y_2) = (0, 3)$  within a  $5\lambda \times 5\lambda$  ROI. In contrast to the linear configuration discussed earlier, the circular layout provides greater spatial diversity, allowing the array to capture and direct signals from a wider range of angles. This setup produces a more balanced radiation pattern, maintaining phase consistency across the aperture while reducing localized power peaks. The circular arrangement also broadens the coverage area and improves interference suppression, showing that maximizing spatial diversity can lead to better beam control and more uniform energy distribution across the field.

Ideally, both amplitude and phase of the complex-valued beamforming weights are incorporated into the distributed in-plane RF holographic aperture to maximally exploit the available degrees of freedom. In this case, coherent combining requires precise synchronization among spatially distributed arrays, which can be achieved via phase alignment between the RF signals transmitted or received by the distributed arrays using two phase-locked optical beams whose offset in frequencies and phase is the desired RF carrier and phase [21], [25].

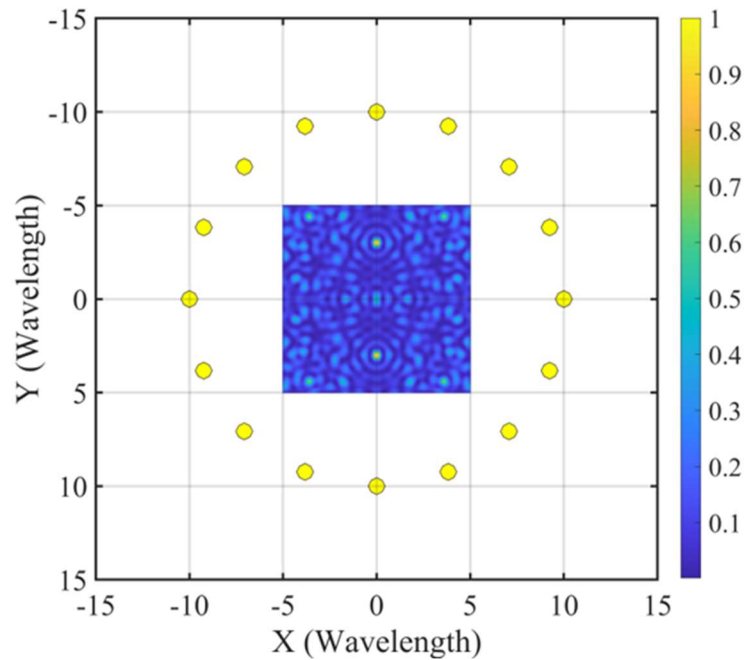


Figure 2.5. Simulation setup showing the normalized power profile (linear scale) for 16 antenna elements uniformly distributed on a circle of radius  $9.35\lambda$  for beamforming analysis.

## **Chapter 3**

### **SYSTEM OVERVIEW**

This chapter presents the RF-photonic system architecture for the transmitter which includes the photonic processing unit (PPU) containing the tunable optical paired source (TOPS) [25] and feed network, followed by the complex weighting matrix, which enables phase and amplitude control in the optical domain to apply beamforming weights and finally the remote RF frontend. This chapter also explains how both phase and frequency coherence are maintained across the system to ensure coherent combining at the user.

#### **3.1 Photonic Processing Unit**

Photonic-enabled coherent distributed transmission system is illustrated in Figure 3.1, where phase coherence is maintained between antennas using an RF-photonic system. By virtue of optical fibers, each antenna can be easily configured in various array formats, in which each channel can be controlled in both amplitude and phase. The adjustable transmit phased-array antenna system uses a photonic processing unit based on a TOPS [25] system to generate and transmit high-quality RF signals across long distances, ensuring that temporal coherence is preserved throughout transmission.

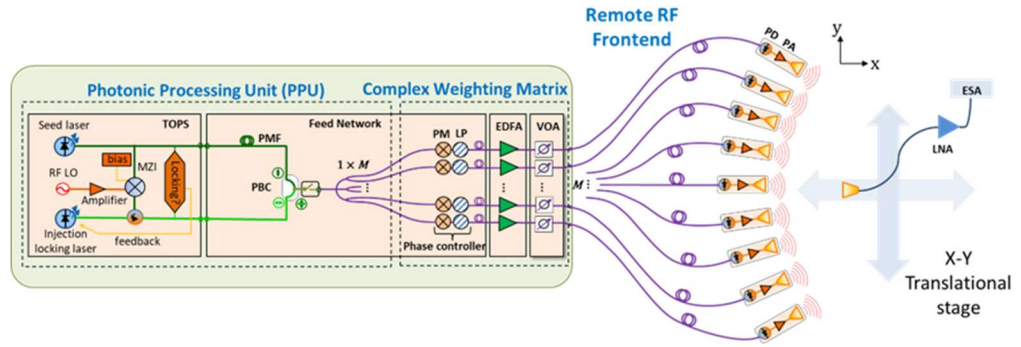


Figure 3.1. System diagram of distributed TX antenna. (TOPS: Tunable Optical Paired Source; LO: Local Oscillator; PMF: Polarization-Maintaining Fiber; PBC: Polarization Beam Combiner; PM: Phase Modulator; LP: Linear Polarizer ; EDFA: Erbium-Doped Fiber Amplifier ; VOA: Variable Optical Attenuator; PD: Photo Detector; PA: Power Amplifier; LNA: Low-Noise Amplifier; ESA: Electronic Spectrum Analyzer).

### 3.1.1 Tunable Optical Paired Source (TOPS)

In this RF-photonic system, the input to the radio-frequency-over-fiber (RFoF) distribution network is two laser signals that have identical optical phase noise, which is realized by using two distributed feedback (DFB) lasers with one injection locked to a modulation sideband derived from the other. Through a combination of thermally tuning the DFBs, and direct tuning of the RF synthesizer that provides the modulation sidebands, the offset frequency between the DFBs can be tuned up to 100 GHz, while the injection-locking synchronization ensures that the beat signal obtained by combining the lasers on a photodiode has a linewidth of  $\sim 1$  Hz [25].

Using this technique, the two correlated but offset optical signals can be fed into a single optical fiber and distributed to remote antennas while preserving the RF temporal coherence over long distributed distances, which has been demonstrated up to 45 km [20]. Furthermore, each antenna is equipped with a high-speed photodetector

[27] that down-converts the two optical signals into the desired RF signal directly at the RF front-end.

### **3.1.2 Feed Network**

In the feed network section, each antenna is driven by the same laser pair, ensuring identical optical sources for all transmission paths. This configuration preserves both temporal and spatial coherence across all antenna feeds, enabling temporally and spatially coherent coordination among all distributed TX array components. Once at the array, the paired optical signal is fed to a fiber-based polarization beam combiner (PBC), where the signals from the lasers are combined into the two orthogonal polarization modes of a polarization-maintaining fiber (PMF). With one wavelength in each of the fiber's linear transverse polarization modes, the total output is comprised of the two laser wavelengths transmitted over a single polarization-maintaining (PM) fiber [28].

## **3.2 Complex Weighting Matrix**

After the feed network section, the output of the polarization beam combiner is split into the  $M$  channel feed network, where each fiber channel corresponds to a different transmit antenna element. As shown in Figure 3.1, in the complex weighting matrix section, a low-speed lithium niobate (LN) phase modulator is used with each channel to impart a controlled RF phase for each element. Because the two lasers are in different polarization states when they enter the modulator, they experience a different phase shift for a given voltage to the EOM electrodes. This is due to the anisotropy of the electro-optic effect in lithium niobate (LN) [29]

After that a 45-degree keyed connector rotates the polarization alignment of the PM fiber by 45 degrees and a linear fiber polarizer is used to limit the output energy to only that guided by the fiber's slow axis. Each path also includes a VOA along with the aforementioned phase modulator to enable control of both the RF phase and amplitude. While the LN phase modulators used in this work provide frequency-independent phase shifts, their maximum time delay is limited to pico-seconds, which necessitates the use of alternate true-time-delay (TTD) methods for broadband operation. That being said, the single-frequency setup used in this work does not require a TTD network, however, incorporating such a network is a planned future direction for the broadband operation of our system.

### 3.3 Remote RF Frontend

The  $M^{\text{th}}$  optical signal is subject to an appropriate complex weighting, analogous to precoding [30], and then down-converted and amplified before being sent to each antenna element. The RF signal is then transmitted using high power photodetectors (PDs) [27], an optional power amplifier following each PD, and standard antennas, with the optical signal converted into an electrical signal using a high-power PD. The  $M$  transmit antenna elements collaborate to generate a multidimensional in-plane RF hologram on the image plane via coherent beam combining.

## **Chapter 4**

### **EXPERIMENTAL BUILDING BLOCKS**

This chapter presents the hardware integration and software development to evaluate the practical performance of phase-synchronized distributed beamforming systems. It details the implementation of the transmitter (Tx) module, including both the software framework developed in LabVIEW and the hardware enhancements achieved through the integration of supplementary test equipment for improved data acquisition and system monitoring. To enable future experimental studies, custom true time delay (TTD) modules and a dedicated anechoic testing environment are also designed and assembled. A detailed overview of these developments is provided in the following sections of this chapter.

#### **4.1 Transmitter Cart Software Overhaul**

This Tx module is reconstructed from an earlier setup to establish a more efficient and scalable system. While the earlier configuration contained valuable hardware components, the accompanying control software lacked flexibility and is no longer compatible with new functionalities. To overcome these limitations, a new LabVIEW-based interface is developed, as illustrated in Figure 4.1. This redevelopment enhanced data acquisition speed, operational stability, and overall system performance. In addition, new capabilities such as automated calibration, synchronized device control, and real-time performance monitoring are implemented.

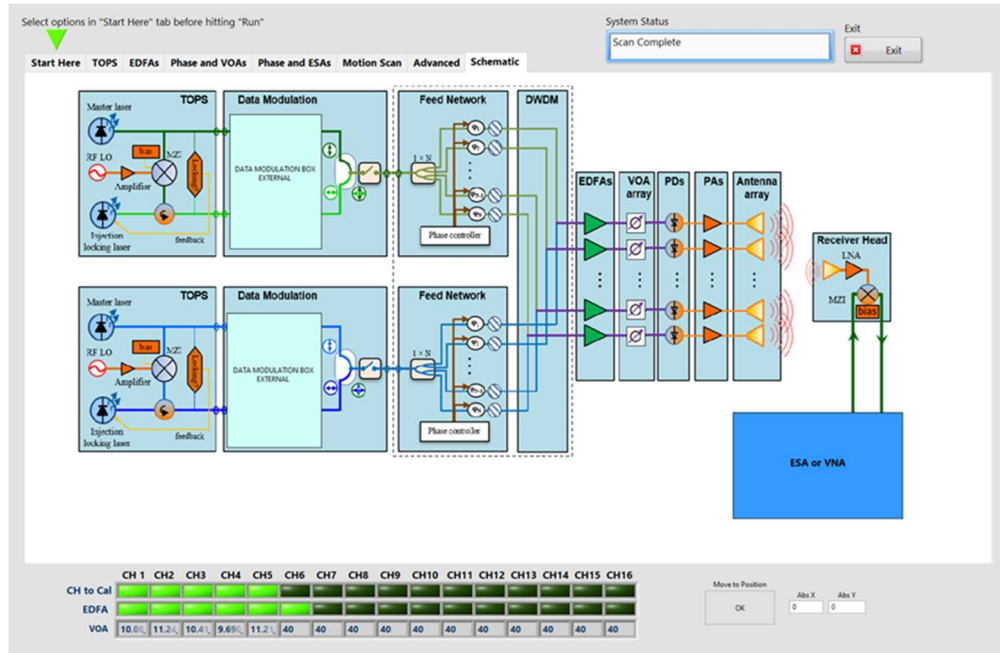


Figure 4.1. Schematic diagram of the TX system in the LabVIEW interface.

The redesigned LabVIEW interface-illustrated in Figure 4.2, is developed to improve usability and optimize overall system operation. During the overhaul, over forty unnecessary case structures are removed, and several overlapping routines are merged to make the program more efficient and easier to interpret. The updated framework reduces excessive layering of code, resulting in a smoother and faster execution process. It is based on a producer-consumer model, where commands triggered by user actions or automated events are distributed to separate processing loops dedicated to the UI, data acquisition, EDFA, and TOPS systems. This modular design enables simultaneous task execution, simplifies troubleshooting, and supports seamless incorporation of new capabilities. Adding new functions now requires only minimal coding-typically the creation of an associated control, event handler, and

process case-therby shortening development time and improving long-term maintainability.

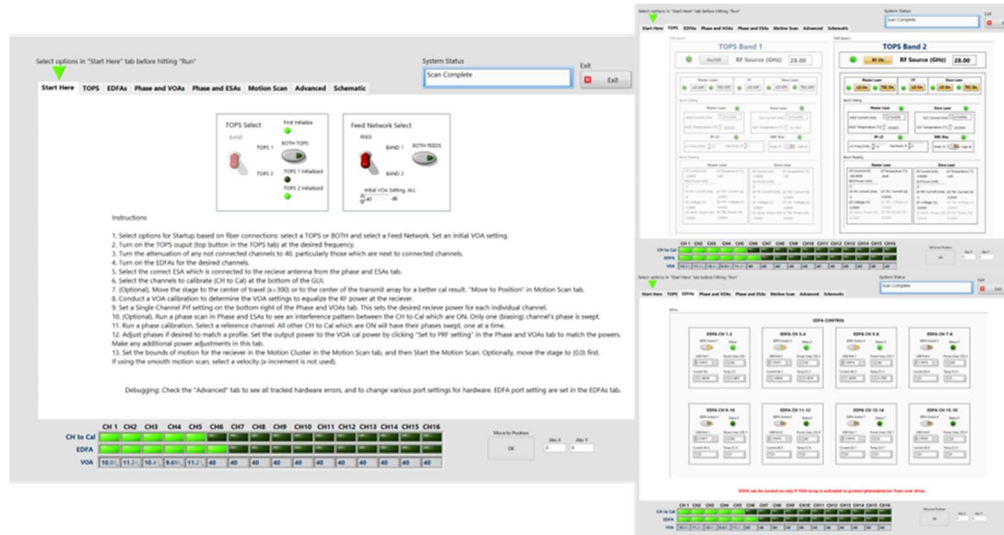


Figure 4.2. LabVIEW “Start Here” panel showing initialization options for TOPS and feed networks, channel calibration selection, and motion control setup for the transmitter unit.

The front panel layout is redesigned to organize related functionalities more intuitively and to keep key system indicators visible at all times. This updated configuration improves usability and allows the operator to monitor overall system status more effectively. One example is shown in Figure 4.3, the “Phase and VOAs” tab, which provides control for tuning the phase shifters and VOAs. This panel also includes the VOA calibration module, where attenuation values are automatically scanned to balance the output power of each active transmitter element. Another important interface, the “Phase and ESAs” panel, features the phase calibration

section, which aligns the phase of all non-reference channels with the designated reference channel to ensure uniform phase across the antenna array.

The remapped code also includes many new features, including automated data collection. The “Motion Scan” tab includes the ability to do a stepped or smooth motion scan with the receive antenna and to record all the power measurements to a spreadsheet. An auto set button was added to automatically identify the ideal center frequency for the electronic spectrum analyzer (ESA). The ability to change the speed of the stage is added to speed up or slow down data acquisition. Additionally, an improved shutdown sequence is implemented which automatically turns off all the optical amplifiers and lasers when the program is stopped, whether by error or by the user. The shutdown sequence improves safety of the equipment and user. Besides the current features, space is allocated in the diagram to add other instruments for data acquisition. The code is designed in such a way so that changing to a different instrument should be relatively straightforward.



Figure 4.3. LabVIEW panel showing phase and amplitude calibration control panels used to adjust VOAs and synchronize phase across all transmitter channels.

## 4.2 Transmitter Hardware Fixes and Testing

The Tx cart adapted for this project is in generally good condition, with most hardware components functioning as expected. However, several issues emerged during initial testing, including polarization misalignment and inactive channels. Each channel is carefully examined to identify and correct the underlying problems. Most of these issues are traced to fiber-related faults such as contaminated connector ends, loose connections, and incorrect channel mapping. These are resolved by thoroughly cleaning all connectors, ensuring secure connections, and labeling previously unmarked fibers for future reference.

Additional challenges involved the photodiodes responsible for converting optical signals into microwave transmissions. Because these devices are extremely fragile, failures can occur through multiple mechanisms. To mitigate further damage, 40-GHz modified uni-travelling carrier (MUTC) PDs are used which are mounted on custom-designed printed circuit boards (PCBs) equipped with protective biasing and short-circuit safeguard circuits as shown in Figure 4.4. The photodiodes are coupled to the tapered slot antennas (TSAs) using 3D-printed protective holders for mechanical stability. Electrostatic discharge (ESD) precautions are also implemented during handling. With these improvements, the Tx system is now fully operational and capable of beamforming across all sixteen channels.

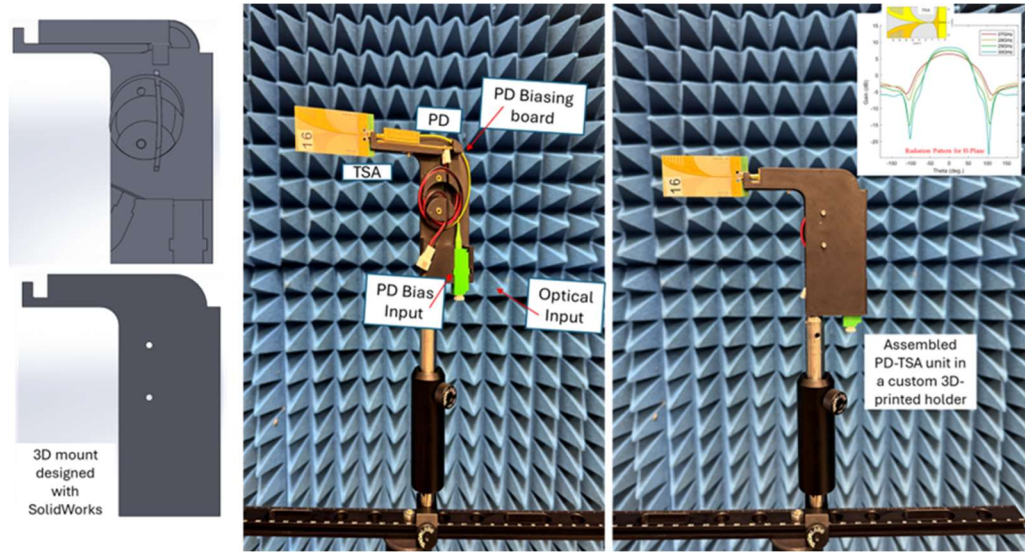


Figure 4.4. Assembled PD and TSA antenna unit in a custom 3D printed holder with antenna radiation pattern.

### 4.3 True Time Delay (TTD) Units

Currently, the Tx system uses phase modulators as phase shifters to generate the complex amplitude and phase distribution on the array elements. A common phase shift over a wide signal bandwidth causes beam squint, a phenomenon that can be remedied by TTD, which imposes the same time delay for all frequency components within the wideband signal. To have the capability to test the difference between TTDs and phase shifters, we assembled two TTD boxes which each contain 8 TTDs and their control electronics. These optical TTDs have motorized turning mirrors inside which can be used to adjust the optical path. The actual TTDs themselves are legacy hardware that was not previously being used. They have a maximum delay of 1,120 ps, or 34 cm. The long maximum delay is made possible by the devices being double pass, meaning that the same port is used for the input and output. To

accommodate the single port devices, we purchased fiber circulators and spliced them to the delay lines.

To enable integration of the time delays into the system, we designed mounting fixtures and a sheet metal enclosure. The mounting fixtures are 3D printed, and each one fits a delay line and the excess fiber. The fixtures are then mounted on the sheet metal enclosure. The enclosure is designed to fit 8 delay lines and fit into a typical 19" rack, including the current system cart. It is designed in Protocase Designer and manufactured by Protocase. Photos of the enclosure are shown in Figure 4.5. The assembly is done over the course of a week, including cable management.



Figure 4.5. Left: A true time delay (TTD) box with lid on. Right: inside view of the enclosure.

The delay lines are tested to ensure that the electronic controls work. Each delay line is assigned to a serial port, and those ports correspond to labeled fibers. The serial control of the delay lines works, and each TTD has acceptable insertion loss and total length (including the fiber pigtailed). The two rack-mount cases can be added to our current transmitter cart if we remove an unused unit. In the future, we will test them in the system to see if being able to continuously scan over a large range of

phases (instead of  $-\pi$  to  $\pi$ ) will make a difference. Additionally, maybe the TTDs will beamform better than the phase shifters when used with wider band signals, or there may be some benefit to using both together.

#### **4.4 Anechoic Enclosure Plan and Build**

To conduct communication-based experiments using the distributed RF-photonics transmitter system, it is essential to have an anechoic enclosure that allows multiple antenna arrays to be arranged over a wider spatial region. This setup minimizes external reflections, interference and multipath effects, enabling accurate assessment of beamforming and signal distribution performance under controlled conditions. Following these aspects, an anechoic enclosure is designed and constructed. To maximize safety and minimize the build time, absorptive walls are chosen to make, but not the floor or the ceiling. That way, the structure does not have to be fully enclosed (a fire hazard). Additionally, if the system is far enough from the floor and ceiling, path loss should be enough to prevent significant multipath effects.

To build the enclosure, room dividers, foam boards, absorber panels, and Velcro are used. The room dividers are 6 feet tall and 6 feet wide, separated into 3 sections each. The white foam boards are 6 feet tall and 4 feet wide. The absorber panels are 2 ft by 2 ft, 9 of them fit on each room divider and 8 of them fit on each foam board. Absorbers are bought from dB absorber in California due to the low lead time and competitive price. Polyurethane pyramidal absorber is chosen with 100 mm tall pyramids, to optimize absorption at our target frequencies ( $>10$  GHz) and limit the size and weight of the absorbers. Some additional absorbers are ordered to place on a test table to further limit reflections. Velcro is glued to the back of the panels and affixed Velcro tape to the dividers. They can be removed, and the enclosure can be

collapsed if necessary. Figure 4.6 shows a picture of the completed enclosure after test equipment setup is moved in.

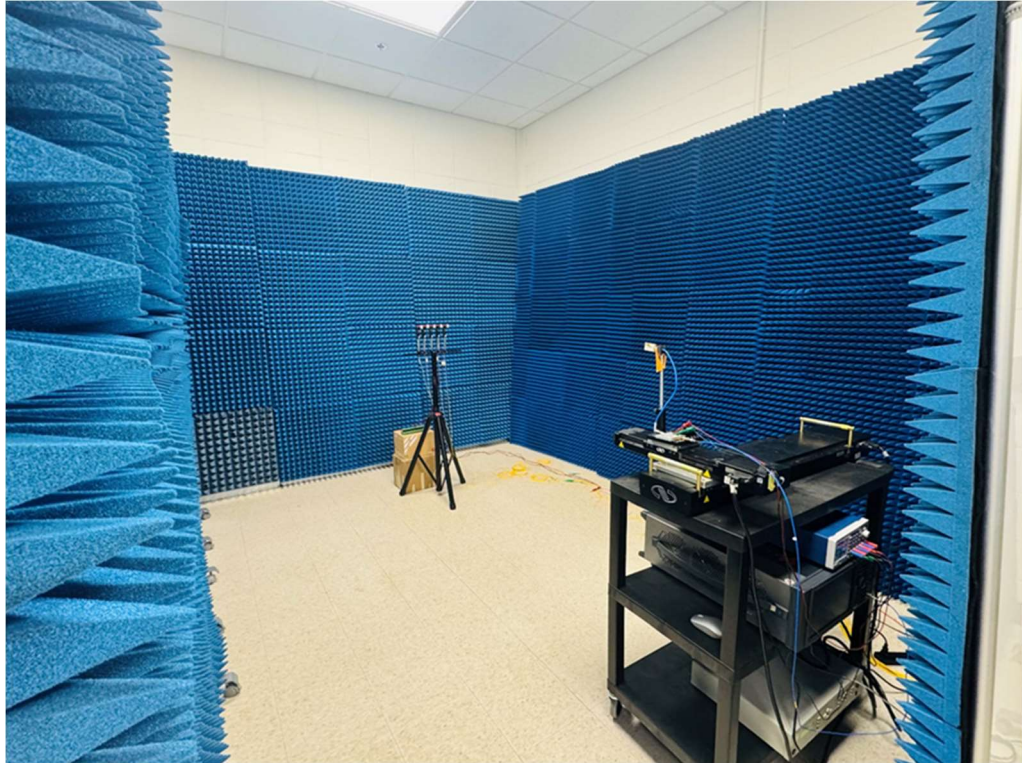


Figure 4.6. Anechoic enclosure made from foam boards, movable room dividers, pyramidal microwave absorber and antenna setup.

## Chapter 5

### RESULTS AND DISCUSSION

This chapter presents the experimental setup incorporating the key components required for coherent RF signal distribution, including the tunable optical paired source (TOPS) [25] and high-power photodiodes (PDs) [27]. The chapter introduces various calibration techniques used to obtain far-field radiation patterns and to maintain phase coherence across multiple distributed antennas. It also presents a detailed performance analysis demonstrating the formation of in-plane RF holograms, with experimental results compared with simulations.

#### 5.1 Experimental Setup

Proof-of-concept validation for coherent phase distribution over distance is carried out on the over-the-air (OTA) testbed described in the Chapter 3. The experimental setup presented in Figure 5.1 is a simplified version of Figure 3.1. includes the key elements for coherent distribution of RF signals, including the TOPS and high-power PDs. This simplified and reconfigurable hardware is of reduced size, weight, cost, and power consumption and facilitates signal processing in the analog domain. The experimental setup employs five TSAs as transmit antennas, each receiving its signal from a 40-GHz modified uni-travelling carrier (MUTC) PD [27]. At present, five TSA antennas are arranged in a linear array with an element spacing of 2.8 cm. The coherent output signals emitted by the transmit antenna elements results in the generation of a radiation pattern that corresponds to the intended in-plane RF hologram pattern.

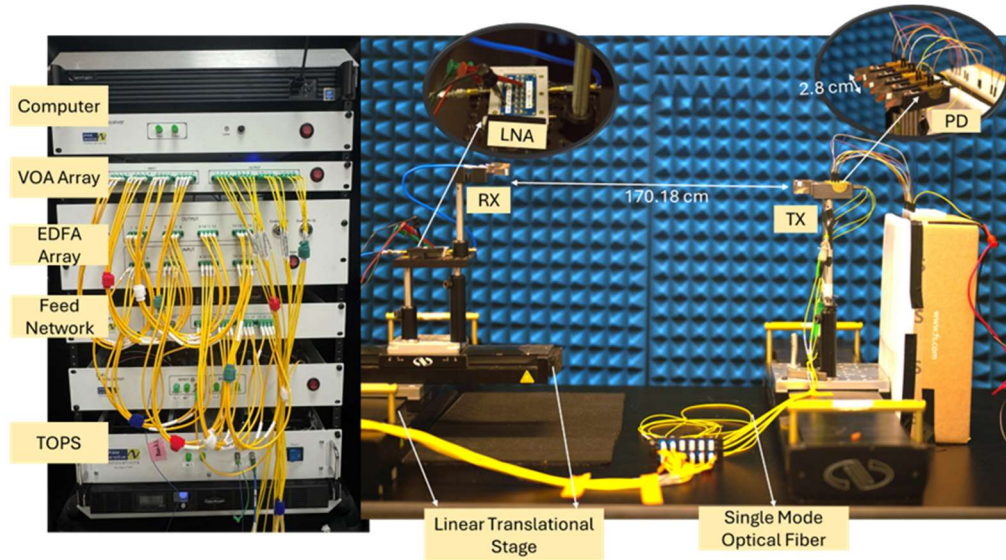


Figure 5.1. System measurement setup for the experimental performance analysis.

An electronic spectrum analyzer (ESA) is used to measure the received signal power, while a TSA receiving antenna, mounted on a linear translational stage, is used to swept along the  $y$ -axis using a LabVIEW-controlled setup to capture the peaks and nulls of the RF fringes parallel to the transmit antennas. Although the current configuration enables one-dimensional scanning, the approach can be extended to full two-dimensional spatial mapping by incorporating additional translational stages.

To direct the holographic pattern to orient a peak or null on the receive antenna, several phase orientations can be computed in terms of voltage and applied to the modulator to produce a phase delay on the RF signal output. In this demonstration, phase-only experiments are performed while maintaining the same amplitudes for all weights. All of the experiments are performed in an indoor laboratory, where a direct line of sight (LOS) is accessible between the transmitter and the receiver.

All simulations are performed using MATLAB, where parameters are selected to be comparable to the experimental values. Five distributed antennas are used in the simulation that represents the hardware configuration of the five antennas. Adjacent element and transmit antenna spacings to the receive antenna are maintained at 2.8 cm and 170.18 cm, respectively, for both simulation and experiment. To illustrate the radiation pattern, the simulation and experiment both consider a linear translational stage of 60 cm along the  $y$ -axis and a carrier frequency of 28 GHz. The simulation parameters are set to match those of the experimental setup, which are summarized in Table 5.1.

Table 5.1 Simulation & Experimental Parameters

<b>Parameter</b>	<b>Value</b>
Carrier frequency	28 GHz
No of transmit antenna	5
No of receive antenna	1
Antenna element spacing	2.8 cm
Propagation distance	170.18 cm
Scan length along the axis	60 cm

## 5.2 Interference Pattern for Various Phase Distributions

To demonstrate RF phase coherence among five distributed antennas, different phase configurations are applied to the transmit antennas and the combined radiation patterns are captured in the image plane for validation. The measured optical power and current levels at key points of the system are summarized in Table 5.2, corresponding to the components illustrated in Figure 3.1.

Table 5.2 Measured Power and Current Levels at System Key Points

System Block	Parameter	Value
Seed Laser Output (TOPS)	Optical Power	+18 dBm
Injection Locking Laser (TOPS)	Optical Power	+16.8 dBm
Feed Network Output (per channel)	Optical Power	-2.80 dBm
VOA Output (per channel)	Optical Power	+7.50 dBm
PD Output (per channel)	DC Current	+12 mA

The scan, depicted in Figure 5.2(a) illustrates the uninterrupted fringe pattern for the five in-phase transmitters, maintaining the same configuration as in the experimental setup. The measured extinction ratio ranged from 15 to 25 dB, suggesting a generally even power distribution among the sources. In Figure 5.2(b), five transmit antennas with alternating phase values ( $0^\circ$ ,  $180^\circ$ ,  $0^\circ$ ,  $180^\circ$ ,  $0^\circ$ ) are used to

demonstrate that phase coherence is preserved, and the extinction ratio remains comparable to Figure 5.2(a).

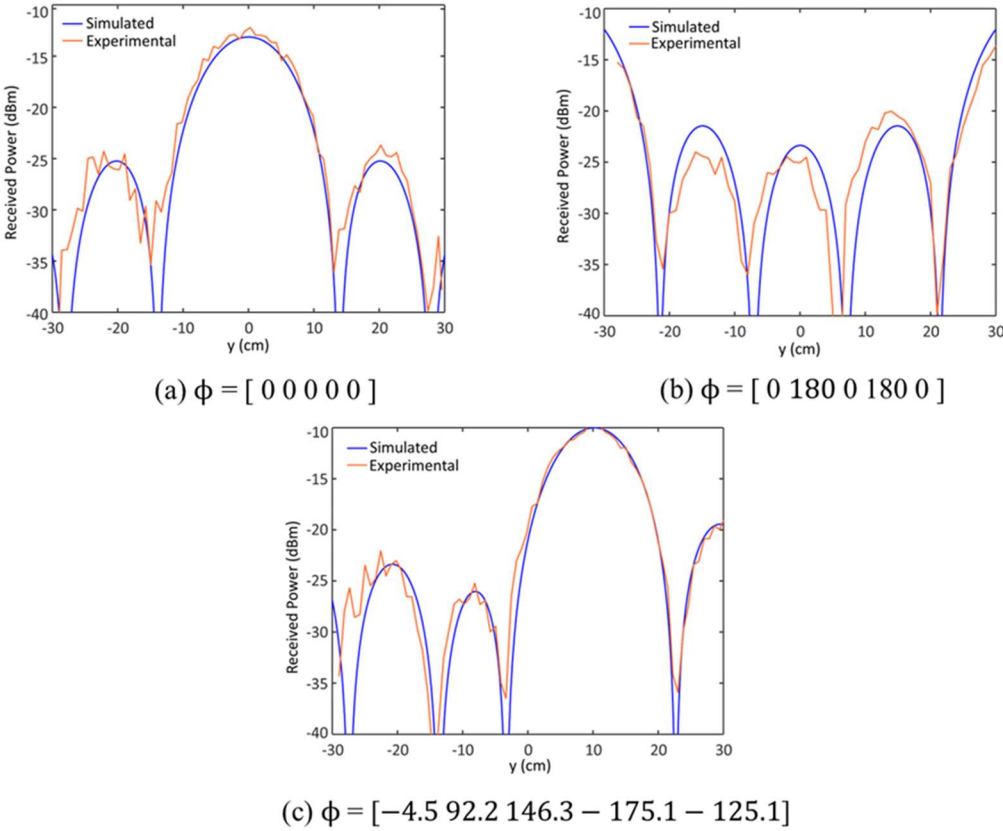


Figure 5.2. Performance comparison between simulation and lab experiment in terms of interference pattern for various phase ( $\phi$ ) distributions in degrees.

In Figure 5.2(c) complex conjugate beamforming is used to determine the phase, allowing for the demonstration of the coherent combining of the five transmit signals. The phases are calculated in such a way that the beam is formed at 10 cm along the  $y$ -axis. The slight mismatch between the simulated and experimental results is attributed to multipath effects arising from environmental reflections within the

laboratory, which are known to affect interference patterns at millimeter-wave frequencies.

### 5.2.1 $V_{2\pi}$ Estimation & Measurement

The true  $V_{2\pi}$  of the phase modulator is a critical parameter for implementing beamforming in practice, as the applied voltage must produce the desired phase shift for accurate beam steering. To determine this value, a least-squares estimation approach is applied. Specifically, for each applied voltage, the radiation pattern along the linear stage is measured while assuming that the true phase response of the modulator is unknown. The experimentally observed radiation patterns are then compared in terms of least squared error with simulated ones to infer the actual phase corresponding to each voltage input.

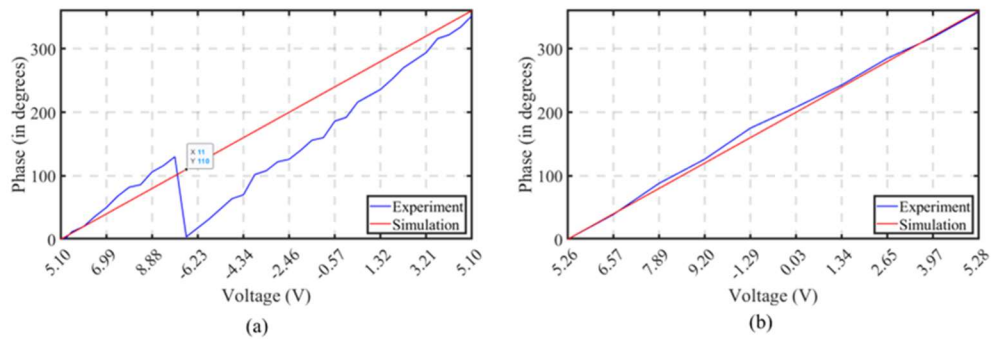


Figure 5.3.  $V_{2\pi}$  measurement based on least squared error estimation; (a)  $2\pi$  phase sweep with incorrect  $V_{2\pi}$  set to the system; (b)  $2\pi$  phase sweep with correct  $V_{2\pi}$  set to the system.

This procedure is repeated over a fine voltage interval spanning more than one full  $360^\circ$  phase cycle to ensure accurate phase mapping. The estimated experimental phases are then plotted alongside the simulated phase response, as illustrated in Figure 5.3(a). By comparing the simulated and measured voltage - phase curves, we obtain the true  $V_{2\pi}$  of the system. After incorporating this estimated  $V_{2\pi}$  value and reapplying the least-squares estimation, the experimental voltage - phase curve is found to closely match the simulated response, confirming the accuracy of the estimated  $V_{2\pi}$  as demonstrated in Figure 5.3(b).

### 5.2.2 Near - field Phase Compensation

During calibration stage, the system has been calibrated using two channels at a time, with the condition that the phases that maximize the received power at the center of the stage are the calibrated phases. This procedure effectively implements MRT, also referred to as conjugate beamforming, at the central point during the phase calibration.

In the far-field, creating a beam at the center requires zero relative phase across the channels. However, in the actual experimental setup, the receiver lies in the near-field, and therefore the calibrated phases that produce a constructive peak at the center are not zero. Consequently, when steering the beam away from the center, it is necessary to compensate for these near-field calibration phases in addition to applying the standard MRT beamforming weights.

This effect is illustrated in Figure 5.4. As shown in Figure 5.4(a), applying MRT beamforming without near-field phase compensation fails to steer the beam. In contrast, Figure 5.4(b) demonstrates that incorporating the compensation enables successful beam steering toward the desired direction.

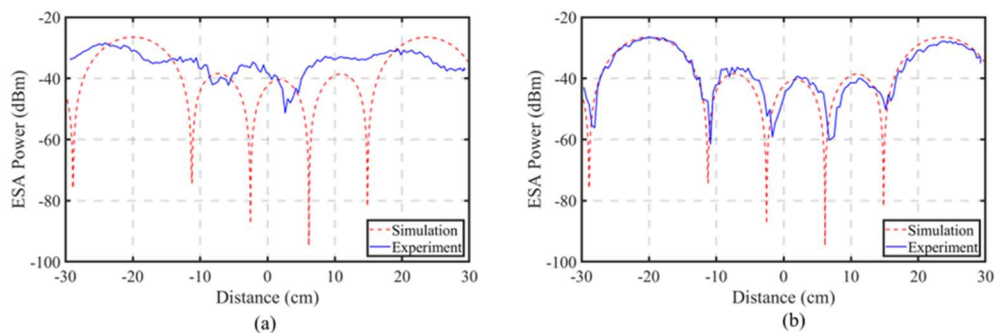


Figure 5.4. Near-field phase compensation; (a) beamforming “without” near-field phase compensation, (b) beamforming “with” near-field phase compensation.

### 5.2.3 Beamforming & Beam Steering at Different location

Figure 5.5 illustrates the experimental demonstration of beamforming and beam steering using five active Tx channels. Beams can be steered using either phase-only weighting or complex weighting utilizing both phase and amplitude; the phase-only approach has been extensively pursued in prior work due to its simplicity and ease of implementation [31], [32], [33], [34]. As complex weighting in the optical domain necessitates a VOA and amplitude calibration, the phase-only solution eliminates this requirement and simplifies design and implementation [20]. These experimental results demonstrate the implementation of MRT, in which the phase weights are calculated based on the beamforming algorithm to steer the beam toward the desired location. The amplitude is kept constant across all transmit antenna elements to ensure uniform power distribution.

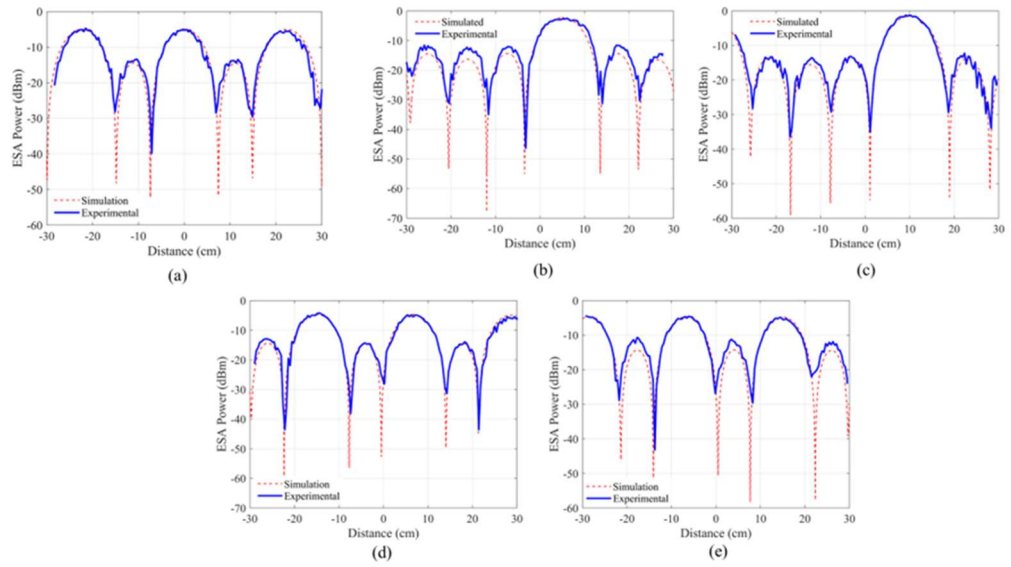


Figure 5.5. Performance comparison between simulation and lab experiment in terms of interference pattern for various beamforming location. (a) beam formed at the center (0 cm); (b) beam steered to +5 cm; (c) beam steered to +10 cm; (d) beam steered to -15 cm; (e) beam steered to +15 cm.

All channels are first-calibrated at the center position ( $y = 0$  cm) in Figure 5.5(a) using the custom LabVIEW control interface, ensuring coherent signal alignment across the array. After calibration, the complex conjugate beamforming algorithm is implemented to direct the main beam toward multiple spatial positions. In Figure 5.5(b) and (c), the beam is electronically steered to  $y = +5$  cm and  $y = +10$  cm. Using the same approach, Figure 5.5(d) and (e) show the beam steered to  $y = -15$  cm and  $y = +15$  cm, allowing direct comparison between the simulated and experimentally measured radiation patterns.

The results confirm consistent steering behavior across the different offsets, validating the accuracy of the phase calibration and the effectiveness of the applied beamforming algorithm. As discussed earlier in the performance comparison results

shown in Figure 5.2, the simulation parameters are configured to match those of the experimental setup, as summarized in Table 5.1. An exception is made for the configuration in Figure 5.5, where the spacing between adjacent elements and the distance between the transmit and receive antennas are increased to 5.08 cm and 200 cm, respectively, in both the simulation and experimental measurements.

### 5.3 Phase Coherence vs Incoherence Transmission across Antennas

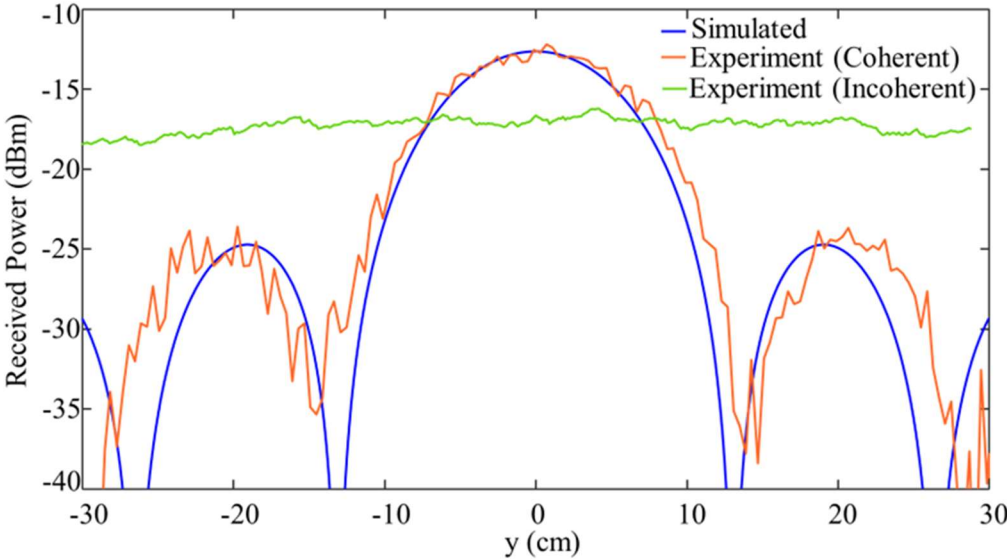


Figure 5.6. Performance comparison showing phase coherence versus incoherence transmission across five TX antennas.

Figure 5.6 compares coherent and incoherent data, where some random phase noise has been introduced into the phase shifters for each of the antenna elements confirming that there are no observed fringe patterns if the sources do not maintain temporal and spatial coherence. The experimental results serve to validate the preservation of phase coherence in distributed antennas, as well as the successful

retrieval of the RF carrier following optical signal propagation to dispersed transmit antennas. Although it is difficult to directly generate and distribute a coherent source at 28 GHz utilizing all electronic technology, the TOPS-produced source is capable of preserving coherence all the way to the antennas.

#### 5.4 Maintenance of Phase Coherence with Differential Fiber Lengths

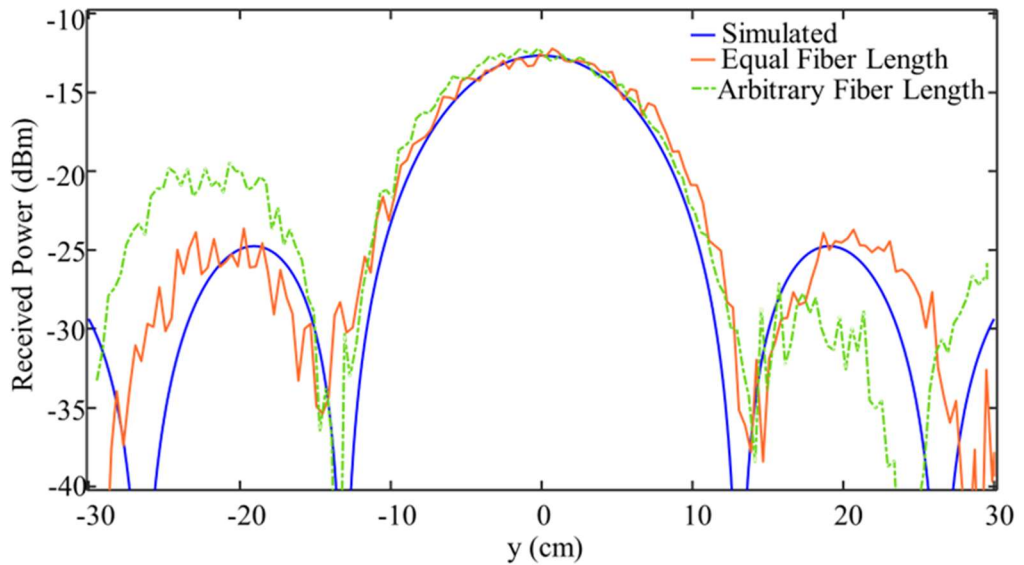


Figure 5.7. Performance comparison showing maintenance of phase coherence with differential fiber lengths.

To demonstrate the preservation of phase coherence across distant distributed antennas, more fibers are added to the link that connect the PDs and the VOA's output. Notably, polarization preservation is not necessary because an optical fiber is used after the polarization states have been combined. To show phase coherence with an arbitrary fiber length, fibers with a length of 100m are added into transmit antennas 3, 4, and 5. The resulting scan is shown by the green trace in Figure 5.7, which

matches the equal-length scan (red trace), apart from some discrepancies in the sidelobe levels. These discrepancies may be attributable to power imbalance between the antennas due to losses induced by the additional fiber connections.

In practical usage any differences in the feed fiber lengths would be fixed and unchanged after initial deployment and thus accounted for in the system calibration. Also, by using phase-stable fiber, we can eliminate any real-time fluctuations. The primary significance of Figure 5.7 is that it illustrates how the transmit antennas maintain their coherent state across different lengths, which is difficult to do with all-RF implementations. As a result, if we can maintain coherence among the antennas within an array, then we can likewise maintain the coherence between the different arrays as well, which enables spatial coherence among distributed phased arrays. The lengths measured in this test were limited by the availability of optical fiber during this experiment. A similar experiment could be conducted to demonstrate the ability to distribute coherent RF signals by using a kilometer-long optical fiber to multiple transmitters while maintaining temporal and spatial coherence, as supported by previous experimental and theoretical studies [20], [35], [36].

## **Chapter 6**

### **FUTURE WORK**

Building upon the promising results and methodologies developed in this thesis for RF-photonic distributed systems, several directions for future research are outlined below:

#### **6.1 Beamforming with Multiple Users in Distributed Antenna System**

Building upon the current proof-of-concept implementation, future work will aim to extend the demonstrated RF-photonic distributed antenna system into a fully scalable cell-free massive MIMO network capable of supporting multiple users simultaneously in both uplink and downlink operation. The present setup utilizes five transmit antennas connected to a central processing unit through optical fiber links, ensuring full phase and frequency coherence across all elements. Subsequent development will focus on deploying a larger number of distributed access points (APs) over a broader area, interconnected through long-distance optical fronthaul, to evaluate large-scale network coordination and performance.

The system is envisioned to operate under a time-division duplexing (TDD) scheme, where uplink pilot signals from users are received by the APs for channel estimation across the distributed network. The estimated channels will be used for coherent signal combining during uplink reception and for precoding-based beamforming in the downlink. The MRT and ZF precoding designs introduced in chapter 2 will be further applied and optimized for multi-user beamforming, enabling

dynamic interference suppression and efficient power allocation. Ultimately, the goal is to transition from a laboratory-scale system to a real-world RF-photonics testbed that demonstrates scalable, high-capacity, and phase-coherent distributed beamforming across extended distance.

## **6.2 Incorporating Data Modulation on the Coherent Optical Carriers**

To enable comprehensive system-level evaluation of the RF-photonics platform, including data rate, spectral efficiency, and bit error rate, a custom data modulation module will be integrated onto the coherent optical carriers. Maintaining phase and frequency coherence between the transmitter and receiver through the photonic link is critical for achieving high spectral efficiency in distributed systems. The envisioned cell-free network aims to deliver uniform SINR across the coverage area, overcoming the limitations of conventional cellular architectures. Furthermore, the coherence preserved by the RF-photonics design facilitates coherent signal combining at the user end, substantially improving overall system throughput and spectral efficiency.

## **Chapter 7**

### **CONCLUSION**

This thesis presents a photonicly enabled distributed multiple input multiple output (MIMO) system designed for the long-range distribution of RF signals without the limitations imposed by conventional RF cabling and power loss. The developed RF-photonic phased-array architecture demonstrates in-plane RF hologram formation, showing that coherent RF signals can be generated and distributed across spatially separated antennas using optical fiber links. The system maintains phase and frequency coherence among multiple transmit antennas, even when differential fiber lengths are introduced, confirming the stability of the photonic synchronization approach.

The work establishes a foundation for scalable and flexible beamforming using photonic signal processing, highlighting how coherence preservation enables precise control of radiation patterns in a distributed network. The techniques explored here illustrate the potential of using photonic architectures for cell-free and wide-area communication systems, where multiple access points can operate coherently under a shared optical reference.

Looking ahead, the system can be extended to support multi-user operation by increasing the number of transmit antennas and integrating data modulation onto the coherent optical carriers. These additions will enable complete system-level performance evaluation, including data rate, spectral efficiency, and bit-error rate (BER). Overall, this research demonstrates a promising step toward realizing scalable,

high-capacity, and phase-coherent distributed RF-phonic networks suitable for next-generation wireless communication platforms.

## REFERENCES

- [1] D. W. Prather *et al.*, “Millimeter-Wave and Sub-THz Phased-Array Imaging Systems Based on Electro-Optic Up-Conversion and Optical Beamforming,” *IEEE J. Select. Topics Quantum Electron.*, vol. 29, no. 5: Terahertz Photonics, pp. 1–14, Sept. 2023, doi: 10.1109/JSTQE.2023.3306953.
- [2] Y. Xing and T. S. Rappaport, “Propagation Measurement System and Approach at 140 GHz-Moving to 6G and Above 100 GHz,” in *2018 IEEE Global Communications Conference (GLOBECOM)*, Abu Dhabi, United Arab Emirates: IEEE, Dec. 2018, pp. 1–6. doi: 10.1109/GLOCOM.2018.8647921.
- [3] J. A. Nanzer, S. R. Mghabghab, S. M. Ellison, and A. Schlegel, “Distributed Phased Arrays: Challenges and Recent Advances,” *IEEE Trans. Microwave Theory Techn.*, vol. 69, no. 11, pp. 4893–4907, Nov. 2021, doi: 10.1109/TMTT.2021.3092401.
- [4] “5G Moves into the Light: Holographic Massive MIMO | IEEE Communications Society.” Accessed: June 05, 2023. [Online]. Available: <https://www.comsoc.org/publications/ctn/5g-moves-light-holographic-massive-mimo>
- [5] Z. Wang *et al.*, “A Tutorial on Extremely Large-Scale MIMO for 6G: Fundamentals, Signal Processing, and Applications,” *IEEE Commun. Surv. Tutorials*, vol. 26, no. 3, pp. 1560–1605, 2024, doi: 10.1109/COMST.2023.3349276.
- [6] S. I. Chowdhury *et al.*, “Two-Dimensional Radio-Frequency Holography Using Distributed Apertures,” in *2024 IEEE Conference on Computational Imaging Using Synthetic Apertures (CISA)*, Boulder, CO, USA: IEEE, May 2024, pp. 01–05. doi: 10.1109/CISA60639.2024.10576473.
- [7] N. Hassan and X. Fernando, “Massive MIMO Wireless Networks: An Overview,” *Electronics*, vol. 6, no. 3, p. 63, Sept. 2017, doi: 10.3390/electronics6030063.
- [8] X.-H. You, D.-M. Wang, B. Sheng, X.-Q. Gao, X.-S. Zhao, and M. Chen, “Cooperative distributed antenna systems for mobile communications [Coordinated and Distributed MIMO,” *IEEE Wireless Commun.*, vol. 17, no. 3, pp. 35–43, June 2010, doi: 10.1109/MWC.2010.5490977.
- [9] I. F. Akyildiz and J. M. Jornet, “Realizing Ultra-Massive MIMO (1024x1024) Communication in the (0.06–10) Terahertz Band”.

- [10] S. A. Busari, K. M. S. Huq, S. Mumtaz, L. Dai, and J. Rodriguez, “Millimeter-Wave Massive MIMO Communication for Future Wireless Systems: A Survey,” *IEEE Commun. Surv. Tutorials*, vol. 20, no. 2, pp. 836–869, 2018, doi: 10.1109/COMST.2017.2787460.
- [11] H. Q. Ngo, A. Ashikhmin, H. Yang, E. G. Larsson, and T. L. Marzetta, “Cell-Free Massive MIMO Versus Small Cells,” *IEEE Trans. Wireless Commun.*, vol. 16, no. 3, pp. 1834–1850, Mar. 2017, doi: 10.1109/TWC.2017.2655515.
- [12] L. Cheng *et al.*, “Coordinated Multipoint Transmissions in Millimeter-Wave Radio-Over-Fiber Systems,” *J. Lightwave Technol.*, vol. 34, no. 2, pp. 653–660, Jan. 2016, doi: 10.1109/JLT.2015.2480786.
- [13] S. Shi *et al.*, “Photonically Assisted 2-D Transmit Array Using Fourier-Optic-Based Beamformer,” *IEEE Transactions on Microwave Theory and Techniques*, pp. 1–9, 2025, doi: 10.1109/TMTT.2025.3581547.
- [14] D. W. Prather *et al.*, “Fourier-Optics Based Opto-Electronic Architectures for Simultaneous Multi-Band, Multi-Beam, and Wideband Transmit and Receive Phased Arrays,” *IEEE Access*, vol. 11, pp. 18082–18106, 2023, doi: 10.1109/ACCESS.2023.3244063.
- [15] A. Ishimaru, “Theory of unequally-spaced arrays,” *IRE Transactions on Antennas and Propagation*, vol. 10, no. 6, pp. 691–702, Nov. 1962, doi: 10.1109/TAP.1962.1137952.
- [16] K. C. Kerby and J. T. Bernhard, “Correction to ‘Sidelobe Level and Wideband Behavior of Arrays of Random Subarrays,’” *IEEE Transactions on Antennas and Propagation*, vol. 55, no. 1, pp. 250–250, Jan. 2007, doi: 10.1109/TAP.2006.888479.
- [17] N. Jin and Y. Rahmat-Samii, “Advances in Particle Swarm Optimization for Antenna Designs: Real-Number, Binary, Single-Objective and Multiobjective Implementations,” *IEEE Transactions on Antennas and Propagation*, vol. 55, no. 3, pp. 556–567, Mar. 2007, doi: 10.1109/TAP.2007.891552.
- [18] J. A. Nanzer, “Spatial filtering of grating lobes in mobile sparse arrays,” in *2016 IEEE Radio and Wireless Symposium (RWS)*, Jan. 2016, pp. 26–28. doi: 10.1109/RWS.2016.7444354.
- [19] J. Bai *et al.*, “Optically Driven Ultrawideband Phased Array With an Optical Interleaving Feed Network,” *IEEE Antennas and Wireless Propagation Letters*, vol. 13, pp. 47–50, 2014, doi: 10.1109/LAWP.2013.2295917.
- [20] C. Harrity *et al.*, “Tunable Optically Fed Radiofrequency Source for Distributing Coherent High-Fidelity Signals,” in *2024 IEEE/MTT-S International Microwave Symposium - IMS 2024*, June 2024, pp. 86–89. doi: 10.1109/IMS40175.2024.10600269.

- [21] S. I. Chowdhury *et al.*, “Coherently distributed RF antenna arrays using photonic links,” *Opt. Express*, vol. 33, no. 17, p. 36919, Aug. 2025, doi: 10.1364/OE.562685.
- [22] D. Prather, S. Shi, G. Schneider, X.-F. Qi, C. Schuetz, and J. Murakowski, “Simultaneous Multi-Band, Multi-Beam, and Multi-Function TX/RX Phased Array Systems,” in *2022 IEEE International Symposium on Phased Array Systems & Technology (PAST)*, Waltham, MA, USA: IEEE, Oct. 2022, pp. 1–6. doi: 10.1109/PAST49659.2022.9974976.
- [23] D. Prather *et al.*, “Optically Upconverted, Spatially Coherent Phased-Array-Antenna Feed Networks for Beam-Space MIMO in 5G Cellular Communications,” in *Optical Fiber Communication Conference (OFC) 2023 (2023), paper W4J.4*, Optica Publishing Group, Mar. 2023, p. W4J.4. doi: 10.1364/OFC.2023.W4J.4.
- [24] S. I. Chowdhury *et al.*, “Photonic-enabled holographic MIMO with multiple coherently distributed antennas,” in *Terahertz, RF, Millimeter, and Submillimeter-Wave Technology and Applications XVIII*, SPIE, Mar. 2025, pp. 56–60. doi: 10.1117/12.3043921.
- [25] G. J. Schneider, J. A. Murakowski, C. A. Schuetz, S. Shi, and D. W. Prather, “Radiofrequency signal-generation system with over seven octaves of continuous tuning,” *Nature Photonics*, vol. 7, no. 2, pp. 118–122, Feb. 2013, doi: 10.1038/nphoton.2012.339.
- [26] H. Yang and T. L. Marzetta, “Performance of Conjugate and Zero-Forcing Beamforming in Large-Scale Antenna Systems,” *IEEE Journal on Selected Areas in Communications*, vol. 31, no. 2, pp. 172–179, Feb. 2013, doi: 10.1109/JSAC.2013.130206.
- [27] A. Beling, X. Xie, and J. C. Campbell, “High-power, high-linearity photodiodes,” *Optica*, vol. 3, no. 3, pp. 328–338, Mar. 2016, doi: 10.1364/OPTICA.3.000328.
- [28] G. J. Schneider *et al.*, “Multiuser-MIMO Transmitter Based on Optical Polar-Vector Modulators,” *IEEE Photonics Technology Letters*, vol. 30, no. 21, pp. 1834–1837, Nov. 2018, doi: 10.1109/LPT.2018.2868248.
- [29] D. W. Prather *et al.*, “Optically Upconverted, Spatially Coherent Phased-Array-Antenna Feed Networks for Beam-Space MIMO in 5G Cellular Communications,” *IEEE Trans. Antennas Propagat.*, vol. 65, no. 12, pp. 6432–6443, Dec. 2017, doi: 10.1109/TAP.2017.2735549.
- [30] T. Parfait, Y. Kuang, and K. Jerry, “Performance analysis and comparison of ZF and MRT based downlink massive MIMO systems,” in *2014 Sixth International Conference on Ubiquitous and Future Networks (ICUFN)*, July 2014, pp. 383–388. doi: 10.1109/ICUFN.2014.6876818.

- [31] F. R. Castella and D. L. Marable, "Optimized planar array antenna nulling with phase only control," in *1993 23rd European Microwave Conference*, Sept. 1993, pp. 886–888. doi: 10.1109/EUMA.1993.336739.
- [32] S. T. Smith, "Optimum phase-only adaptive nulling," *IEEE Transactions on Signal Processing*, vol. 47, no. 7, pp. 1835–1843, July 1999, doi: 10.1109/78.771033.
- [33] D. A. Day, "Fast phase-only pattern nulling for large phased array antennas," in *2009 IEEE Radar Conference*, May 2009, pp. 1–4. doi: 10.1109/RADAR.2009.4976945.
- [34] A. J. Abdulkader, J. Mohammed, and R. H. Thaher, "Phase-Only Nulling with Limited Number of Controllable Side Elements," 2020. Accessed: Nov. 04, 2025. [Online]. Available: <https://www.semanticscholar.org/paper/Phase-Only-Nulling-with-Limited-Number-of-Side-Abdulkader-Mohammed/dc7f43d86ccef87f2801c57d6fafbc8ed356bca7>
- [35] S. Shi *et al.*, "Conformal Wideband Optically Addressed Transmitting Phased Array With Photonic Receiver," *Journal of Lightwave Technology*, vol. 32, no. 20, pp. 3468–3477, Oct. 2014, doi: 10.1109/JLT.2014.2317191.
- [36] S. Galli *et al.*, "A Novel Opto-Electronic Architecture for Large Multi-Band and Multi-Beam Phased Arrays," in *2019 IEEE Wireless Communications and Networking Conference (WCNC)*, Apr. 2019, pp. 1–7. doi: 10.1109/WCNC.2019.8886063.

## Appendix

### PUBLICATION LIST

1. S. I. Chowdhury *et al.*, “Two-Dimensional Radio-Frequency Holography Using Distributed Apertures,” in *2024 IEEE Conference on Computational Imaging Using Synthetic Apertures (CISA)*, Boulder, CO, USA: IEEE, May 2024, pp. 01–05. doi: 10.1109/CISA60639.2024.10576473.
2. S. I. Chowdhury *et al.*, “Coherently distributed RF antenna arrays using photonic links,” *Opt. Express*, vol. 33, no. 17, p. 36919, Aug. 2025, doi: 10.1364/OE.562685.
3. S. I. Chowdhury *et al.*, “Photonically-enabled holographic MIMO with multiple coherently distributed antennas,” in *Terahertz, RF, Millimeter, and Submillimeter-Wave Technology and Applications XVIII*, SPIE, Mar. 2025, pp. 56–60. doi: 10.1117/12.3043921.